Combined 60° Wide-Field Choroidal Thickness Maps and High-Definition En Face Vasculature Visualization Using Swept-Source Megahertz OCT at 1050 nm

Kathrin J. Mohler,[1] Wolfgang Draxinger,[1] Thomas Klein,[1] Jan Philip Kolb,[1,2] Wolfgang Wieser,[1] Christos Haritoglou,[3] Anselm Kampik,[4] James G. Fujimoto,[5] Aljoscha S. Neubauer,[4] Robert Huber,[1,2] and Armin Wolf[4]

[1]Lehrstuhl für BioMolekulare Optik, Fakultät für Physik, Ludwig-Maximilians-Universität München, Munich, Germany
[2]Institut für Biomedizinische Optik, Universität zu Lübeck, Lübeck, Germany
[3]Augenklinik Herzog Carl Theodor, Munich, Germany
[4]Augenklinik der Ludwig-Maximilians-Universität München, Munich, Germany
[5]Department of Electrical Engineering and Computer Science and Research Laboratory of Electronics, Massachusetts Institute of Technology, Cambridge, Massachusetts, United States

Correspondence: Armin Wolf, Augenklinik der Ludwig-Maximilians-Universität München, Campus Innenstadt, Mathildenstraße 8, D-80336 München, Germany; armin.wolf@med.uni-muenchen.de.

Submitted: February 12, 2015
Accepted: July 28, 2015

Citation: Mohler KJ, Draxinger W, Klein T, et al. Combined 60° wide-field choroidal thickness maps and high-definition en face vasculature visualization using swept-source Megahertz OCT at 1050 nm. *Invest Ophthalmol Vis Sci*. 2015;56:6284–6293. DOI:10.1167/iovs.15-16670

Purpose. To demonstrate ultrahigh-speed swept-source optical coherence tomography (SS-OCT) at 1.68 million A-scans/s for choroidal imaging in normal and diseased eyes over a ~60° field of view. To investigate and correlate wide-field three-dimensional (3D) choroidal thickness (ChT) and vascular patterns using ChT maps and coregistered high-definition en face images extracted from a single densely sampled Megahertz-OCT (MHz-OCT) dataset.

Methods. High-definition, ~60° wide-field 3D datasets consisting of 2088 × 1024 A-scans were acquired using a 1.68 MHz prototype SS-OCT system at 1050 nm based on a Fourier-domain mode-locked laser. Nine subjects (nine eyes) with various chorioretinal diseases or without ocular pathology are presented. Coregistered ChT maps, choroidal summation maps, and depth-resolved en face images referenced to either the retinal pigment epithelium or the choroidal–scleral interface were generated using manual segmentation.

Results. Wide-field ChT maps showed a large inter- and intraindividual variance in peripheral and central ChT. In only four of the nine eyes, the location with the largest ChT was coincident with the fovea. The anatomy of the large lumen vessels of the outer choroid seems to play a major role in determining the global ChT pattern. Focal ChT changes with large thickness gradients were observed in some eyes.

Conclusions. Different ChT and vascular patterns could be visualized over ~60° in patients for the first time using OCT. Due to focal ChT changes, a high density of thickness measurements may be favorable. High-definition depth-resolved en face images are complementary to cross sections and thickness maps and enhance the interpretation of different ChT patterns.

Keywords: choroid, choroidal thickness maps, en face vasculature visualization, optical coherence tomography, swept-source OCT, Megahertz OCT, wide-field imaging

The choroid may play an important role in the pathogenesis of several diseases,[1,2] such as age-related macular degeneration (AMD),[3] central serous chorioretinopathy (CSCR),[4] and diabetic retinopathy,[5] due to the high choroidal blood flow and its adjacent location to the affected retinal pigment epithelium (RPE) and retina. With the choroid supplying the essential nutrients and the oxygen to the outer retinal layers,[1] the status of the choroid is likely to have a crucial influence on the course of disease. Additionally, alterations of the RPE are, for example, often associated with changes of the choriocapillaris, and both appear to be affected early in various disease processes.[3–5]

Over the years, optical coherence tomography (OCT)[6] has become a well-established noninvasive imaging modality for investigating the retina in vivo. Using OCT, however, it is more challenging to image the choroid than the retina because of its location posterior to the highly scattering RPE. After the development of two new retinal OCT modalities, enhanced depth imaging spectral-domain OCT (EDI SD-OCT)[7] and swept-source OCT (SS-OCT) at ~1050 nm wavelengths,[8–10] providing enhanced visualization of choroidal vasculature,[7,8,11,12] it has recently become possible to study the choroid more extensively in vivo.[2] In contrast to fundus photography, fluorescein angiography, and indocyanine green angiography (ICGA), OCT not only generates two-dimensional (2D) projections, but also provides depth-dependent information enabling choroidal thickness (ChT) measurements and depth-resolved visualization of choroidal vasculature.

Previous studies on ChT measurements have shown a high interindividual variance in the subfoveal ChT, even for normal eyes.[13–18] Subfoveal ChT is not only negatively correlated with age[13–15,18] but also shows a correlation with the refractive error (RE),[14] the axial eye length,[16] and the diurnal cycle.[17] Furthermore, ChT exhibits a high topographic variance over the posterior pole,[13–15,18,19] suggesting that subfoveal measure-

ments alone may not yield representative results. Volumetric measurements have therefore been performed to generate ChT maps.[20–23] Using 36° field of view ChT maps, Haas et al.[23] correlated areas exhibiting reticular pseudodrusen with local choroidal thickening. These local changes in thickness observed within, but also outside of, the macular region and the topographic variance of ChT over the posterior pole imply that the evaluation of an even larger field of view may be of interest for investigating abnormalities of ChT and vascular patterns in diseased eyes.

With an axial resolution of a few micrometers, different choroidal vascular layers can be examined independently using OCT B-scans and depth-resolved en face OCT images.[24–29] Ferrara et al.[28] and Flores-Moreno et al.[29] compared choroidal vascular abnormalities in depth-resolved en face images of CSCR patients and AMD patients, respectively, with findings obtained from ICGA, and illustrated that depth-resolved en face images provide complementary information to OCT cross sections and other imaging modalities.

However, high-quality en face OCT images require dense A-scan sampling over the entire imaging field of view. Since eye motion limits the maximum acquisition time in ophthalmic imaging, the A-scan rate of the system restricts the field of view that can be acquired in high-definition en face images to ~20° for most commercial OCT devices. Recently, prototype SS-OCT systems have been demonstrated with A-scan rates up to several MHz,[30–33] enabling the acquisition of densely sampled volumetric datasets spanning larger fields of view.[34]

This pilot study employed an ultrahigh-speed 1050 nm prototype SS-OCT system, operating at 1.68 million A-scans/s imaging rates, to demonstrate the feasibility of wide-field choroidal imaging over a ~60° field of view for the first time in both normal subjects and patients with a cross section of chorioretinal diseases. The wealth of information provided by our volumetric high-definition wide-field MHz-OCT datasets is illustrated by combined choroidal vasculature visualization and three-dimensional (3D) ChT measurements performed over a field of view comparable to standard fundus photography. Different wide-field ChT patterns were investigated, and the corresponding ChT maps were correlated with coregistered, high-definition, depth-resolved en face images and OCT cross sections visualizing the choroidal anatomy.

Methods

Study Population and 1050 nm MHz-OCT System

In this pilot study, we investigated the potential of high-definition wide-field choroidal imaging by visualizing and analyzing ChT and vascular patterns in six patients (two females and four males, mean age 52.2 years, ranging from 29 to 77 years) with different kinds of chorioretinal diseases and three age-matched normal subjects (three males, mean age 50.7 years, ranging from 31 to 78 years) without ocular pathology, who were part of a patient cohort enrolled in a more general study investigating MHz-OCT imaging at the Augenklinik der Ludwig-Maximilians-Universität (LMU) München.

To acquire densely sampled, wide-field volumetric datasets, we employed an ophthalmic 1050 nm prototype SS-OCT system based on a rapidly wavelength-tunable Fourier-domain mode-locked (FDML) laser.[10,35,36] The details of this custom FDML MHz-OCT system, operating at an ultrahigh A-scan rate of 1.68 MHz, are described in other publications.[32,33,35,37]

The sweep bandwidth was ~65 nm centered at 1050 nm, providing an axial resolution of 15 μm in air. The measured sensitivity was 90 dB with 1.6 mW power incident on the eye, which is consistent with the American National Standards Institute (ANSI) standards for safe ocular exposure.[38] The research adhered to the tenets of the Declaration of Helsinki, and all necessary approvals, including the ethics committee approval granted by the Ethikkommission der Medizinischen Fakultät der LMU München, were obtained for this study, which was registered under Eudramed CIV-13-02-009703 and listed in the WHO study registry. Written informed consent was obtained from all subjects prior to OCT imaging.

In addition to OCT imaging, all patients underwent clinical ophthalmic examination including measurements of refraction, best-corrected visual acuity, and slit-lamp biomicroscopy as well as funduscopic evaluation. All nine subjects (spherical equivalent REs between −8 and +2.25 diopters [D]) had clear optic media and good fixation during OCT examination, so that the image quality was sufficiently high to allow for ChT measurements over the entire ~60° imaging field of view. Only one eye per subject was included to avoid any intraindividual correlations. There was no specification of disease as part of the inclusion criteria since the purpose of this pilot study was to provide an overview of existing wide-field ChT and vascular patterns, including myopic changes, rather than examining a specific disease in detail. However, to avoid deteriorations and a corresponding bias of the ChT assessments, none of the subjects had clinically evident scarring of the retina or choroid associated with panretinal photocoagulation or retinal degenerative diseases within the ~60° imaging field of view.

Wide-Field ChT Maps and Depth-Resolved En Face Images

The imaging procedure has been described previously,[37] and the data analysis is illustrated in Figure 1 for a normal subject, showing clearly visible vascular structures from the RPE to the choroidal–scleral interface (CSI). As an example of a diseased eye, a subject with retinoschisis is presented in Supplementary Figure S1. Wide-field volumetric OCT datasets (Fig. 1A, Supplementary Fig. S1A) were acquired in 1.85 seconds and consisted of 2088 × 1024 A-scans covering a ~60° field of the posterior ocular fundus. The positions of the RPE and the CSI were determined manually by a trained observer (Fig. 1C, Supplementary Fig. S1C) in a subset of the 1024 B-scans (Fig. 1B, Supplementary Fig. S1B) using custom software to handle multi-gigabyte datasets. Choroidal thickness was manually determined at least every 750 μm, but depending on the local anatomy, the observer increased the density of thickness measurements on certain fundus locations whenever it was necessary to reveal even small thickness changes. Interpolation was performed between the segmentation points to create ChT (Fig. 1E, Supplementary Fig. S1E) and summation maps (Fig. 1D, Supplementary Fig. S1D). The latter represent projections of the intensity data from the RPE to the CSI and were overlaid onto the thickness maps to correlate changes in ChT with the corresponding vascular patterns (Fig. 1F, Supplementary Fig. S1F). Complementary to the summation maps showing the entire choroid, the segmentation results also enable the extraction of coregistered depth-resolved choroidal en face images (Figs. 1G–I, Supplementary Figs. S1G–I) from the densely sampled 3D datasets referenced to either the RPE or the CSI. Vascular structure can be visualized in a depth-resolved manner by projecting the intensity data over ~25 μm in depth and generating en face images with different distances to the reference layers. The high transverse sampling density also

Investigative Ophthalmology & Visual Science

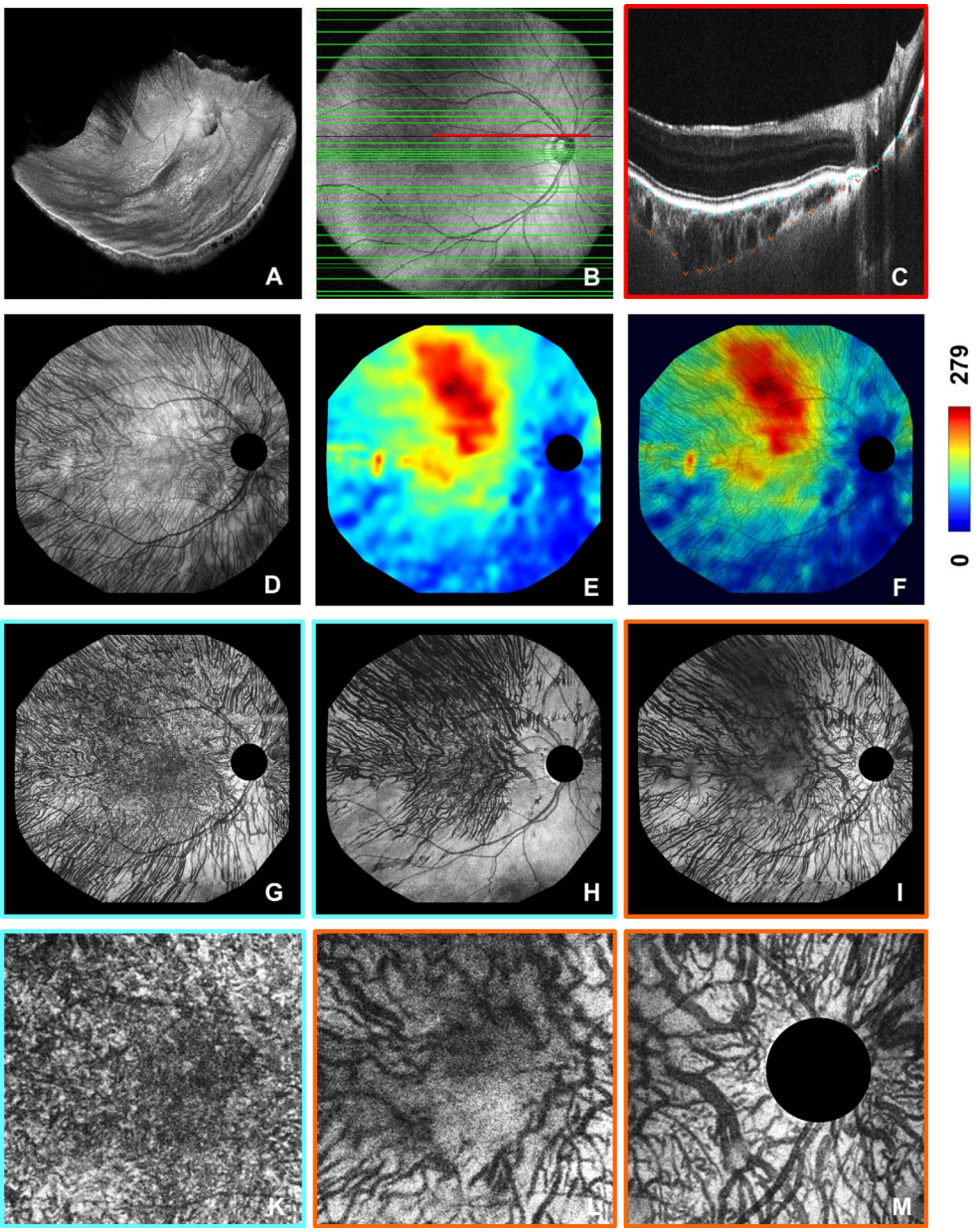

FIGURE 1. ~60° choroidal thickness and vascular pattern visualization using a single densely sampled wide-field OCT dataset of a 78-year-old normal male (spherical equivalent refraction +1.25 D). (**A**) 3D visualization, (**B**) OCT fundus image showing the locations of the B-scans selected for manual choroidal thickness (ChT) measurements (*green lines*), (**C**) close-up view of one of the selected B-scans for which the positions of the retinal pigment epithelium (RPE) (*cyan arrows*) and the choroidal–scleral interface (CSI) (*orange arrows*) were manually determined. Choroidal summation map (**D**) and coregistered choroidal thickness (ChT) map (**E**) resulting from the manual thickness measurements. (**F**) Choroidal summation map overlaid onto the ChT map to enhance the interpretation of the observed ChT pattern. (**G**, **H**) Depth-resolved en face images (thickness ≈ 25 μm) referenced to the manually determined RPE and extracted 25 μm and 75 μm below the RPE to visualize different choroidal vascular structures. (**I**) En face image (thickness ≈ 25 μm) referenced to the CSI and extracted 10 μm above the reference layer. (**K**) Close-up view of the ~20° macular region of image in (**G**). (**L**) Close-up view of the ~20° macular region of image in (**I**). (**M**) Close-up view of a ~20° region centered at the optic nerve head and extracted from the image in (**I**) (choroidal thickness was measured in μm).

enabled the extraction of close-up views to analyze fine details of the vasculature (Figs. 1K–M).

RESULTS

To illustrate the importance of wide-field choroidal imaging, MHz-OCT datasets covering a ~60° field of view are compared to the standard 20° images in Figure 2. In Figures 3 and 4, wide-field ChT and vascular patterns are analyzed independently, before the results are finally combined in Figure 5.

Wide-Field Choroidal Imaging in Comparison to the Standard 20° Field of View

Figure 2 shows a comparison of OCT fundus images (left column), ChT maps (center), and choroidal summation maps (right column) over ~20° and ~60° fields of view in two subjects. Subject 1 was a 63-year-old male with retinal vascular

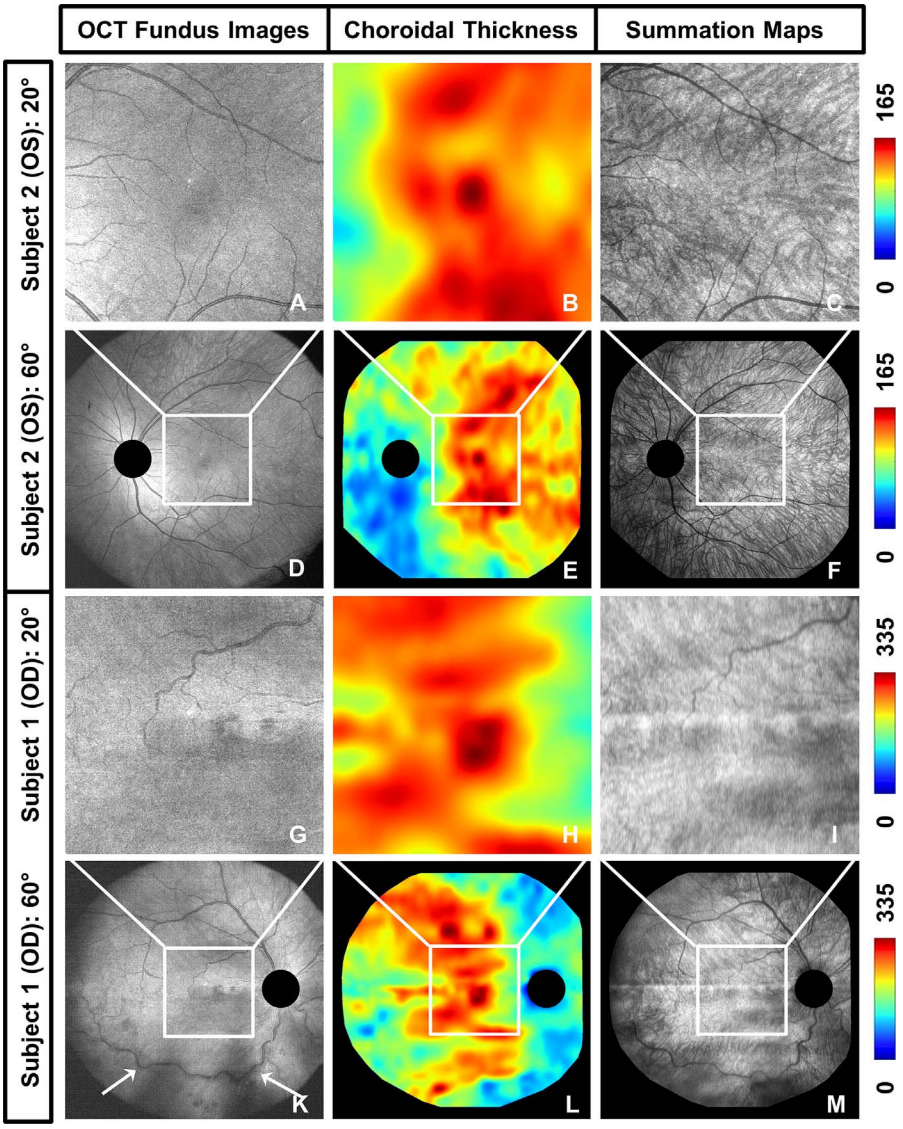

Figure 2. Additional information provided by wide-field choroidal imaging in comparison to conventional 20° field of view imaging. (**A–F**) OCT fundus images, ChT maps, and choroidal summation maps showing the left eye of a 34-year-old male diagnosed with retinoschisis (subject 2, spherical equivalent refraction −1.75 D) over a ∼20° field of view (**A–C**) and a ∼60° field of view (**D–F**). (**G–M**) OCT fundus images, ChT maps, and choroidal summation maps showing the right eye of a 63-year-old male with retinal vascular occlusion (subject 1, spherical equivalent refraction +0.5 D) over a ∼20° field of view (**G–I**) and a ∼60° field of view (**K–M**). The wide-field images show the detailed ChT and choroidal vascular patterns outside of the macular region and enable examination of the entire region affected by the retinal vascular occlusion in subject 1 (*white arrows*) (choroidal thickness was measured in μm).

occlusion, whereas subject 2 was a 34-year-old male with retinoschisis. A large difference in maximum ChT was observed, which may be disease related since it did not reflect the usual age dependence of ChT.

In contrast to the absolute thickness values, the patterns of the 20° macular ChT maps, extracted from the wide-field datasets, show a high degree of similarity with the largest ChT located close to the fovea and similar thickness patterns observed around the fovea. The wide-field ChT maps also show similar thickness distributions but with some noticeable local differences, such as two locations of focal thickening superior to the macular region in subject 1 with retinal vascular occlusion. The wide-field thickness maps also reveal that ChT in the periphery does not seem to follow a clear trend with respect to distance to the fovea. There exist regions of peripheral choroidal thickening, as well as areas of choroidal thinning, so that in general, a high topographic variance in ChT could be observed in the periphery. According to Figure 2, it seems as if the peripheral distribution of ChT may be related to the 20° pattern, since choroidal thickening in adjacent areas to the central 20° may influence central thickness. However, as indicated by the examples given, the overall ChT pattern does not seem to be completely determined by the pattern observed in the macular region. A clear difference between the two patients could further be noticed when examining the vessel structures, with tortuous retinal vessels for subject 1. The OCT fundus images of subject 1 show that the region affected by the retinal vascular occlusion extends beyond the macular region, illustrating the value of wide-field imaging.

These results suggest that thickness maps covering a larger field of view may be important for investigating the choroid and that choroidal vascular structures should be analyzed simultaneously to correlate areas of choroidal thickening or

Investigative Ophthalmology & Visual Science

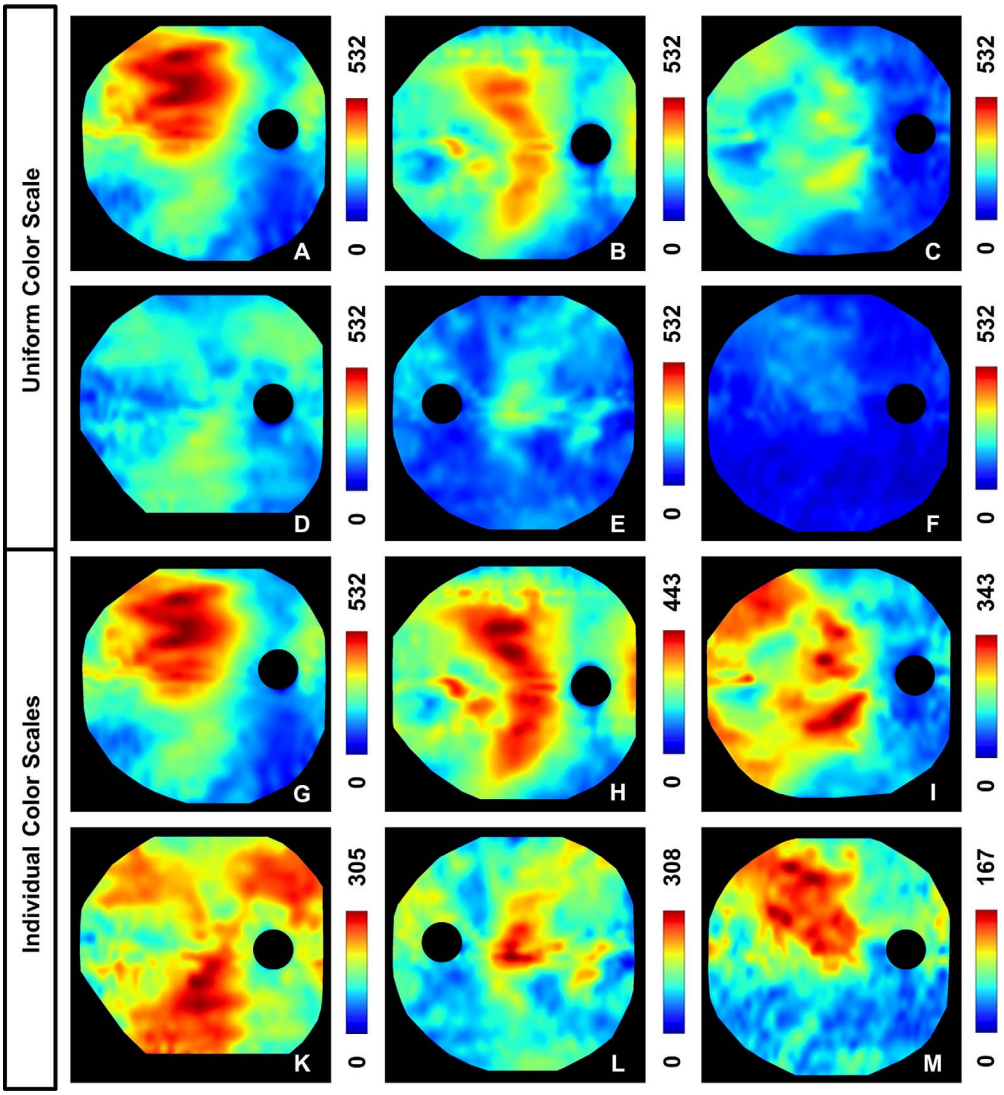

Figure 3. Choroidal thickness (ChT) maps of six different subjects. (**A**–**F**) A uniform color scale is applied on all six subjects to show the high variance in actual ChT; the images are ordered according to decreasing maximum ChT. (**G**–**M**) Individually adapted color scales, normalized with respect to the individual maximum ChT, are employed to visualize the symmetric and asymmetric topographic ChT patterns. (**A**, **G**) 43-year-old normal male (spherical equivalent refraction [SER] −4.75 D), (**B**, **H**) 35-year-old male diagnosed with Graves' orbitopathy and an acute inflammation of the orbit (SER 0 D), (**C**, **I**) 31-year-old normal male (SER 0 D), (**D**, **K**) 29-year-old female with myopia and equatorial degenerations (SER −8 D), (**E**, **L**) 77-year-old female with macular pucker (SER +2.25 D), (**F**, **M**) 75-year-old male diagnosed with AMD (SER −0.75 D). All subjects showed thinning inferonasally to the ONH (choroidal thickness was measured in μm).

thinning with corresponding alterations in vessel structure and thereby enhance the interpretation of ChT maps.

Variance in ChT and Different Color Scales

Figure 3 presents an overview of six different ChT patterns observed among the nine eyes for which wide-field thickness maps were generated. In the images in Figures 3A through 3F, the same color scale was used for all six eyes to analyze the actual ChT. The ChT maps were ordered according to decreasing maximum ChT, and a large variance of ChT was observed among these six subjects with a maximum ChT ranging from 167 to 532 μm. The generated wide-field ChT maps over a ∼60° field of view showed an even larger variance than the 20° thickness maps. Although the subjects in both Figures 3A and 3F show a thickening of the choroid in the superotemporal direction, the 43-year-old male normal subject (Fig. 3A), with a maximum ChT of 532 μm, has a larger ChT throughout the entire posterior pole than the 75-year-old male (Fig. 3F) (maximum ChT of 167 μm) diagnosed with AMD. One of the possible reasons for this difference could be the decrease in ChT with age.[13–15,18] Choroidal thickness varied not only between different subjects but also intraindividually depending on the topographic location.

However, because of the large interindividual variance in wide-field choroidal imaging, topographic variations are not always easy to identify if this uniform color scale is used (Fig. 3F). Therefore, the color scale was adapted individually to maximize the contrast for each of the subjects in images Figures 3G through 3M in order to study the intraindividual thickness patterns. Interestingly enough, the location with the largest ChT was only at the fovea in four of the nine eyes. To account for any possible segmentation errors and potential overestimations of peripheral ChT due to different incident angles of the scanning beam,[14] the location with the largest ChT was attributed to the fovea if the subfoveal ChT was less

Investigative Ophthalmology & Visual Science

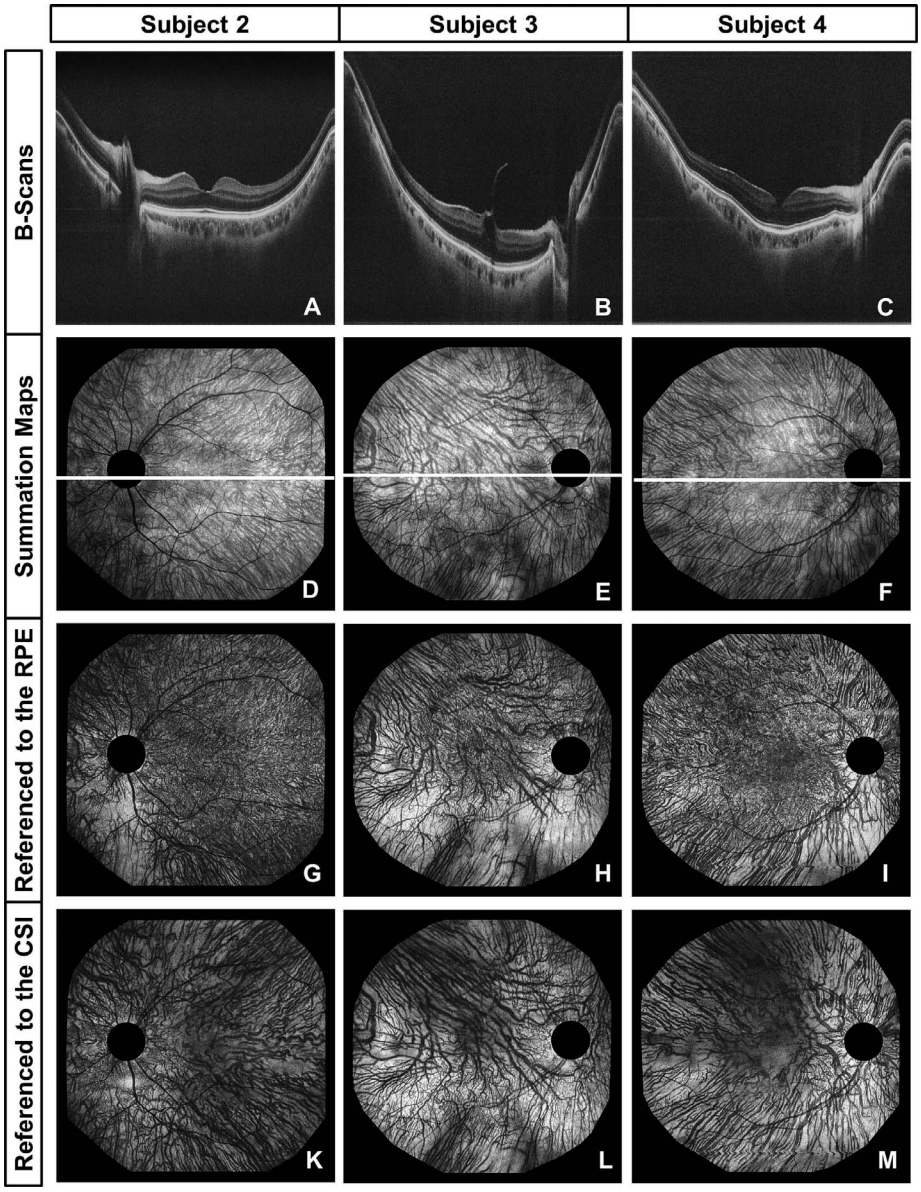

Figure 4. Choroidal vasculature visualization in a 34-year-old male with retinoschisis (subject 2, spherical equivalent refraction (SER) −1.75 D), a 75-year-old male diagnosed with AMD (subject 3, SER −0.75 D), and a normal 78-year-old male (subject 4, SER +1.25 D). B-scans (average of 10 adjacent frames from the same dataset) (**A–C**), choroidal summation maps (**D–F**), and depth-resolved en face images (thickness ≈ 25 μm) referenced to either the RPE (**G–I**) or the CSI (**K–M**) were all extracted from a single densely sampled 3D dataset for each of the subjects and provide complementary information about the asymmetric (subjects 3 and 4) and symmetric (subject 2) patterns of the large lumen choroidal vessels. The en face images referenced to the RPE were extracted 25 μm below the RPE, whereas the en face images referenced to the CSI were extracted 10 μm above the CSI to visualize the vessels with the largest diameter for each fundus location.

than 15% smaller than the maximum ChT observed over the entire imaging field of view.

Although the topographic ChT patterns appear to be quite different, all six subjects show choroidal thinning inferonasally to the optic nerve head (ONH). Three of the eyes (Figs. 3H, 3I, 3L) seem to have a quite symmetrical thickness distribution with respect to the papillomacula axis, so that the inferior and superior sectors show some similarities. However, in the images in Figures 3G and 3M, asymmetric thickness patterns can be observed with a noticeable choroidal thickening in the superotemporal sector. The two ChT maps of normal subjects (Figs. 3G, 3I) suggest that these differences in thickness distribution do not result only from pathologic changes, but that different patterns already exist in normal eyes. Apart from the global pattern, some thickness maps show areas of focal choroidal thickening and thinning (temporal sector in Fig. 3H), suggesting the importance of high-definition scan protocols and high-density thickness measurements for OCT-based investigations of the choroid.

Visualization of Choroidal Vessels Using High-Definition En Face Images

To investigate the origin of the different ChT patterns observed, choroidal anatomy of three different subjects is visualized in Figure 4 using a combination of selected OCT cross sections (Figs. 4A–C), summation maps (Figs. 4D–F), and depth-resolved en face images (thickness ≈ 25 μm), which

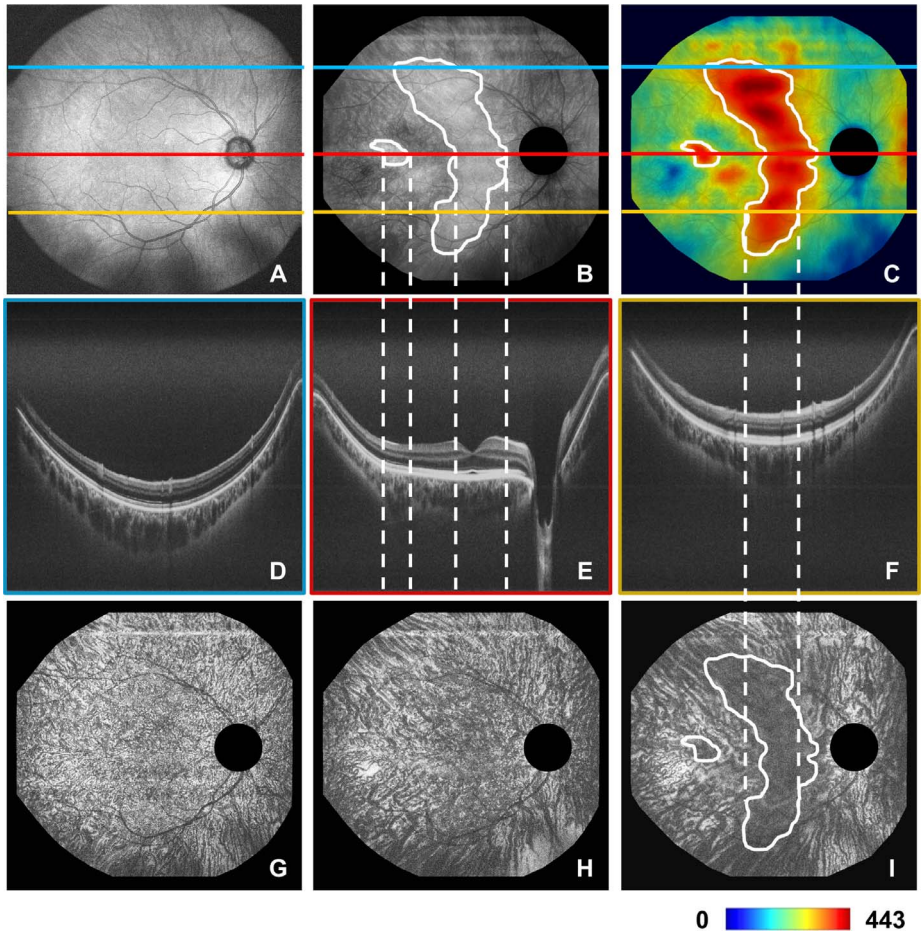

Figure 5. Complementary information provided by the coregistered OCT fundus image (**A**), choroidal summation map (**B**), choroidal thickness (ChT) map (**C**), cross sections (**D**–**F**), and depth-resolved choroidal en face images (thickness ≈ 25 μm) referenced to either the RPE (**G**, **H**) for the inner choroid or the CSI (**I**) for the outer choroid. The depth-resolved en face images referenced to the RPE were extracted 50 μm and 100 μm below the RPE, whereas the en face image using the CSI as a reference layer was extracted 50 μm above the CSI. The B-scans (**D**–**F**) were extracted at the fundus locations marked with the *horizontal blue*, *red*, and *yellow lines* from the same 3D dataset showing the right eye of a 35-year-old male with Graves' orbitopathy and an acute inflammation of the orbit (spherical equivalent refraction 0 D). The main region showing the largest ChT is marked in *white* and corresponds to the fundus locations at which the outer choroidal vessels seem to have the largest diameter. The focal choroidal thickening marked in *white* can be observed consistently on the thickness map, choroidal summation map, and B-scans.

were extracted from the 3D dataset using either the manually determined RPE position (Figs. 4G–I) or CSI position (Figs. 4K–M) as a reference. For each subject, all images were extracted from a single densely sampled wide-field OCT dataset.

Within the choroid, vessels appear dark in OCT cross sections, choroidal summation maps, and en face images.[25] Not all hyporeflective areas in the choroidal summation maps and en face images actually represent choroidal vessels, though, because OCT also has shadowing from retinal vessels. This ambiguity can be resolved by comparing the choroidal summation maps and en face images to coregistered OCT fundus images, which primarily visualize the retinal vessels.

The choroidal summation maps in Figure 4 show different vascular patterns with a relatively symmetric vessel distribution with respect to the papillomacula axis for subject 2 and rather asymmetric patterns for subjects 3 and 4. For the evaluation of the choroidal summation maps, it is important to consider that vessel contrast in regions with larger ChT may be lower than in areas with thin choroid due to signal attenuation with increasing depth. Care must therefore be taken when analyzing choroidal summation maps, since brighter areas (macular region of subject 4) do not necessarily correspond to regions with a low density of choroidal vasculature.

To further investigate these regions, coregistered depth-resolved en face images were extracted from the 3D datasets. To account for the large intraindividual variance in ChT over the posterior pole, the RPE was chosen as a reference layer for the inner choroid, whereas the CSI was used as a reference for visualizing the outer choroid.

The outer choroid could also be displayed using the RPE as a reference, but interpretation of the resulting en face images may be challenging since they may show different layers of the choroid or even the sclera at different fundus locations due to topographic variations in ChT (Fig. 1H versus Fig. 1I). Even the images in Figure 4 (Figs. 4G–I) already show small parts of the sclera in the regions with very small ChT inferonasally to the ONH. We used this method of referencing to the RPE and the CSI, instead of identifying individual choroidal layers, since the indistinct borders between choroidal layers make direct segmentation approaches very challenging while we could directly apply the manual segmentation performed for the ChT measurements.

Throughout the ~60° field of view, an increase in vessel size with depth below the RPE could be observed, which is

consistent with results presented previously.[25] Therefore, the en face images extracted 10 μm above the CSI should depict the vessels with the largest diameter for each fundus location so that the distribution of the maximum vessel size over the posterior pole can be compared to ChT patterns. The en face images reveal in subject 4 that the straight, parallel, large lumen vessels extending from the superotemporal sector to the macular region are not always clearly visualized by the choroidal summation map. In subjects with very thick choroids, even depth-resolved en face images may not enable the visualization of deep choroidal vessels due to low signal at the CSI; but in most cases they can provide complementary information to B-scans, choroidal summation maps, and thickness maps.

Correlation of ChT Maps, Choroidal Summation Maps, En Face Images, and Cross Sections

For each of the patients and normal subjects presented in this paper, the ChT map, the choroidal summation map, the depth-resolved en face images, and the cross sections were all generated from a single densely sampled volumetric OCT dataset. Hence, a direct point-to-point correlation can be used to combine the complementary information provided by the different images and thereby to enhance the interpretation of the ChT maps.

Figure 5 illustrates this approach in the case of a 35-year-old male with Graves' orbitopathy and an acute inflammation of the orbit. Again, an increase in vessel size with depth below the RPE could be visualized employing depth-resolved en face images. While large choroidal vessels can also clearly be delineated on cross sections, en face images are especially useful to visualize the small choroidal vessel of the inner choroid (Fig. 5G) since the high transverse sampling density even enables the generation of enlarged views (Fig. 1K). The ChT map in Figure 5C shows a quite symmetric pattern with respect to the papillomacula axis, with a tendency to a slightly thicker choroid superiorly in comparison to inferiorly. The main region showing the largest ChT is marked in white for comparison with the choroidal summation map (Fig. 5B), the depth-resolved en face images (Figs. 5G–I), and the cross sections (Figs. 5D–F). With a maximum ChT of 443 μm, this patient has a relatively thick choroid, resulting in a quite low signal at the CSI. A comparison of the coregistered ChT and summation maps showed that the regions of large ChT can clearly be correlated with bright areas in the choroidal summation map, where the vessel structure cannot be visualized as clearly as at fundus locations with thinner choroid. Therefore, a depth-resolved en face image (Fig. 5I) referenced to the CSI (extracted 50 μm above this reference layer) and selected cross sections are employed to visualize the large lumen vessels. Comparing the areas between the white vertical bars in the cross sections with the region marked in white in the thickness maps, the area of maximum ChT seems to be correlated with the fundus locations where the vessels show the largest diameter. This observation could consistently be made in the case of a 78-year-old normal subject (Fig. 1) and a 34-year-old male with retinoschisis (Supplementary Fig. S1). Thus, the distribution of the large lumen vessels of the outer choroid seems to play a major role in determining the global ChT pattern. Figure 5 further illustrates that the focal change in ChT, marked in white, could consistently be observed in the ChT map in Figure 5C, the choroidal summation map in Figure 5B, and the B-scan in Figure 5E. The distance between the points of manual measurements, however, sets a lower limit to the size of focal alterations in thickness that can be detected on the ChT maps.

Discussion

In this pilot study, wide-field choroidal OCT imaging at an ultrahigh A-scan rate of 1.68 MHz was demonstrated. To the best of our knowledge, this is the first demonstration of ∼60° wide-field volumetric choroidal imaging in patients, showing that different ChT and choroidal vascular patterns could be visualized simultaneously over a ∼60° field of view in both normal subjects and patients. One of the main advantages of the presented approach is that for each patient and normal subject, the ChT maps and the different kinds of images visualizing the choroidal vasculature were all extracted from a single densely sampled 3D OCT dataset, allowing for a direct point-to-point correlation of features of interest.

Wide-field ChT showed a large inter- and intraindividual variance in peripheral and central ChT, which is consistent with previous studies using thickness maps over smaller fields of view.[20–23] Symmetric and asymmetric ChT patterns and corresponding distributions of the large lumen outer choroidal vessels could be observed in both normal subjects and patients. Hayreh[39] used fluorescein angiography to demonstrate that both the venous and the arterial choroidal vasculature are of a segmental nature with watershed zones isolating the different vascular zones. The locations of these watershed zones showed a large interindividual variation, which may be related to the different vascular patterns observed in our study.

Mori et al.[40] examined the anatomy of choroidal veins using wide-field montage ICGA images and observed symmetric venous vascular patterns in half of the subjects. Most of the remaining subjects with an asymmetric distribution preferentially drained superotemporally, and none of them had an inferonasal preferred drainage route. These results seem to correlate well with the choroidal thickening in the superotemporal direction and the corresponding asymmetric vessel distribution that we observed in three of the nine eyes and the choroidal thinning in the inferonasal direction observed for all nine eyes included in our study. The latter may be due to embryologic development with closure of the eye cup inferonasally.[14,21,40]

This pilot study illustrates the superior information provided by wide-field choroidal imaging using a single densely sampled 3D dataset (in our case 2088 × 1024 A-scans) in comparison to the standard 20° OCT field of view. In our study, densely sampled depth-resolved choroidal en face images and choroidal summation maps were used complementary to B-scans and ChT maps to enhance the interpretation of different thickness patterns. It is possible to obtain wide-field imaging with lower-speed commercial instruments at the expense of reduced A-scan sampling density. However, with lower numbers of A-scans there is the potential risk of missing fine details in choroidal vascular structure.

By increasing the acquisition time from 1.85 to 2.5 seconds, it is possible to enable the acquisition of isotropically scanned datasets consisting of 1900 × 1900 A-scans. Assuming a calculated spot size of approximately 21 μm, our MHz-OCT prototype system could even provide complete gap-free coverage of all resolvable vascular features in the lateral direction according to the Nyquist criterion, which our group has already successfully demonstrated for normal subjects.[32,37] Due to the focal ChT changes observed, a high density of thickness measurements over a wide field of view may also be favorable.

However, the high speed of our system, 16 times faster than the fastest commercial OCT device, also resulted in a decreased sensitivity, since the incident power on the eye (1.6 mW) was kept at the same value as for slower devices. It should be noted, however, that exposure values higher than 1.6 mW

Investigative Ophthalmology & Visual Science

would be acceptable according to ANSI standards due to the fast scanning.

As a first demonstration of 60° MHz-OCT choroidal imaging in patients, only nine individuals are presented here. A more detailed investigation involving a larger study population is ongoing but beyond the scope of this paper. Therefore, only a preliminary estimate on the success rate can be given at this point. So far, 60° ChT maps have successfully been generated for 14 of the 53 subjects enrolled in the MHz-OCT study between October 2013 and March 2014, and for this subgroup, averaging of B-scans from the same dataset yielded a sufficiently high signal for CSI segmentation. However, it would be possible to acquire and average[33] multiple datasets if necessary without significantly extending the time for an OCT examination, since the acquisition time for a single wide-field 3D dataset is only 1.85 seconds. So a higher effective sensitivity could be achieved with our system and might be preferable for future studies, since otherwise patients with thick choroids may be more likely to be unmeasurable due to poor signal at the CSI compared to subjects with thin choroids, potentially introducing a bias.

Based on the OCT fundus images generated for all 53 subjects, vignetting and shadowing caused by the pupil and eyelashes have already been identified as major causes of image quality degradation, affecting approximately half of all subjects and presumably preventing the successful generation of ChT maps over the entire 60° field of view. However, both effects are also known with other wide-field imaging modalities,[41] so strategies exist to overcome these problems.[42] For future studies, the patient interface of our prototype system and the selection of real-time preview images during image acquisition will be optimized to simplify alignment. It is also important to note that usually only parts of the peripheral areas are affected, which we can analyze additionally to the macular region, where ChT is measured conventionally. Hence, we can expect the success rate of ChT maps over a narrower region to be higher.

Optimizing the alignment process, however, will not only reduce image quality degrading effects such as vignetting and shadowing; it will also allow us to place the pivot point of the scanning beam close to the nodal point of the eye more consistently than in this pilot study. Conventionally, the center of the pupil is chosen as the pivot point. For wide-field measurements the nodal point seems to be the best choice, though, since the measurement error caused by an overestimation of peripheral ChT, due to a nonperpendicular incident angle of the OCT beam onto the sample surface at higher viewing angles,[14] will be smaller in this configuration and the curvature of the retina in the OCT images will be reduced.[43] This simplifies the positioning of the retina within our 2.8-mm imaging range in tissue. Assuming an eye length of 24.4 mm,[44] an average ChT of 300 μm, and the location of the pivot point exactly at the nodal point, the maximum angle-dependent measurement error ideally amounts to only approximately 4% for a 60° field of view imaging. The details of this estimation are provided in Supplementary Figure S2.

The study results suggest that the wealth of information provided by densely sampled wide-field OCT might be highly beneficial for early detection of diseases originating from choroidal layers, and that the simultaneous acquisition of ChT maps and depth-resolved en face images aids diagnosis. The results show that different choroidal patterns already exist in normal subjects; but in order to further investigate the origin of different ChT and vascular patterns and to identify potential disease-specific abnormalities, the number of normal subjects and patients per disease should be increased. The time-consuming manual ChT measurements can be replaced by automatic algorithms in the future,[45–48] allowing for data analysis of a larger study population and for potential inclusion of the presented approach in daily clinical practice. Further research will be important to evaluate how dense thickness measurements must be in general to capture all clinically relevant changes. Potentially automatic measurements taking all A-scans into account will not only speed up the whole process but will also provide additional information in some cases, so that the high sampling density of our MHz-OCT system might become essential for thickness measurements and en face visualization alike.

Acknowledgments

We thank Wolfgang Zinth at the Ludwig-Maximilians-Universität München for the support.

Supported by the Gesellschaft der Freunde und Förderer der Augenklinik der Ludwig-Maximilians Universität München eV, the German Research Foundation project OCTLABS (DFG HU1006/3-1), the European Union projects FUN-OCT (FP7 HEALTH, contract no. 201880), the FDML-Raman (FP7 ERC, contract no. 259158), National Institutes of Health (R01-EY011289-28), Air Force Office of Scientific Research (FA9550-10-1-0551 and FA9550-12-1-0499), and by Novartis Pharma GmbH, Nürnberg, Germany. RH and JGF receive royalties for intellectual property owned by MIT and licensed to Carl Zeiss and Optovue. JGF has stock options in Optovue. AW received a research grant from Novartis Pharma GmbH, Nürnberg, Germany.

Disclosure: **K.J. Mohler**, None; **W. Draxinger**, Optores (I); **T. Klein**, Optores (I); **J.P. Kolb**, None; **W. Wieser**, Optores (I), P; **C. Haritoglou**, None; **A. Kampik**, None; **J.G. Fujimoto**, Optovue (I), P; **A.S. Neubauer**, None; **R. Huber**, Optores (I), P; **A. Wolf**, Novartis (F, R)

References

1. Nickla DL, Wallman J. The multifunctional choroid. *Prog Ret Eye Res*. 2010;29:144–168.
2. Mrejen S, Spaide RF. Optical coherence tomography: imaging of the choroid and beyond. *Surv Ophthalmol*. 2013;58:387–429.
3. Bhutto I, Lutty G. Understanding age-related macular degeneration (AMD): relationships between the photoreceptor/retinal pigment epithelium/Bruch's membrane/choriocapillaris complex. *Mol Aspects Med*. 2012;33:295–317.
4. Liew G, Quin G, Gillies M, Fraser-Bell S. Central serous chorioretinopathy: a review of epidemiology and pathophysiology. *Clin Experiment Ophthalmol*. 2013;41:201–214.
5. Cao J, McLeod D, Merges CA, Lutty GA. Choriocapillaris degeneration and related pathologic changes in human diabetic eyes. *Arch Ophthalmol*. 1998;116:589–597.
6. Huang D, Swanson EA, Lin CP, et al. Optical coherence tomography. *Science*. 1991;254:1178–1181.
7. Spaide RF, Koizumi H, Pozzoni MC. Enhanced depth imaging spectral-domain optical coherence tomography. *Am J Ophthalmol*. 2008;146:496–500.
8. Lee EC, de Boer JF, Mujat M, Lim H, Yun SH. In vivo optical frequency domain imaging of human retina and choroid. *Opt Express*. 2006;14:4403–4411.
9. Yasuno Y, Hong Y, Makita S, et al. In vivo high-contrast imaging of deep posterior eye by 1-um swept source optical coherence tomography and scattering optical coherence angiography. *Opt Express*. 2007;15:6121–6139.
10. Huber R, Adler DC, Srinivasan VJ, Fujimoto JG. Fourier domain mode locking at 1050 nm for ultra-high-speed optical coherence tomography of the human retina at 236,000 axial scans per second. *Opt Lett*. 2007;32:2049–2051.
11. Unterhuber A, Povazay B, Hermann B, Sattmann H, Chavez-Pirson A, Drexler W. In vivo retinal optical coherence tomography at 1040 nm - enhanced penetration into the choroid. *Opt Express*. 2005;13:3252–3258.

12. Waldstein SM, Faatz H, Szimacsek M, et al. Comparison of penetration depth in choroidal imaging using swept source vs spectral domain optical coherence tomography. *Eye*. 2015;29:409–415.
13. Margolis R, Spaide RF. A pilot study of enhanced depth imaging optical coherence tomography of the choroid in normal eyes. *Am J Ophthalmol*. 2009;147:811–815.
14. Ikuno Y, Kawaguchi K, Nouchi T, Yasuno Y. Choroidal thickness in healthy Japanese subjects. *Invest Ophthalmol Vis Sci*. 2010;51:2173–2176.
15. Manjunath V, Taha M, Fujimoto JG, Duker JS. Choroidal thickness in normal eyes measured using Cirrus HD optical coherence tomography. *Am J Ophthalmol*. 2010;150:325–329.
16. Li XQ, Larsen M, Munch IC. Subfoveal choroidal thickness in relation to sex and axial length in 93 Danish university students. *Invest Ophthalmol Vis Sci*. 2011;52:8438–8441.
17. Tan CS, Ouyang Y, Ruiz H, Sadda SR. Diurnal variation of choroidal thickness in normal, healthy subjects measured by spectral domain optical coherence tomography. *Invest Ophthalmol Vis Sci*. 2012;53:261–266.
18. Ruiz-Medrano J, Flores-Moreno I, Pena-Garcia P, Montero JA, Duker JS, Ruiz-Moreno JM. Macular choroidal thickness profile in a healthy population measured by swept-source optical coherence tomography. *Invest Ophthalmol Vis Sci*. 2014;55:3532–3542.
19. Ho J, Branchini L, Regatieri C, Krishnan C, Fujimoto JG, Duker JS. Analysis of normal peripapillary choroidal thickness via spectral domain optical coherence tomography. *Ophthalmology*. 2011;118:2001–2007.
20. Esmaeelpour M, Povazay B, Hermann B, et al. Three-dimensional 1060-nm OCT: choroidal thickness maps in normal subjects and improved posterior segment visualization in cataract patients. *Invest Ophthalmol Vis Sci*. 2010;51:5260–5266.
21. Ouyang Y, Heussen FM, Mokwa N, et al. Spatial distribution of posterior pole choroidal thickness by spectral domain optical coherence tomography. *Invest Ophthalmol Vis Sci*. 2011;52:7019–7026.
22. Hirata M, Tsujikawa A, Matsumoto A, et al. Macular choroidal thickness and volume in normal subjects measured by swept-source optical coherence tomography. *Invest Ophthalmol Vis Sci*. 2011;52:4971–4978.
23. Haas P, Esmaeelpour M, Ansari-Shahrezaei S, Drexler W, Binder S. Choroidal thickness in patients with reticular pseudodrusen using 3D 1060-nm OCT maps. *Invest Ophthalmol Vis Sci*. 2014;55:2674–2681.
24. Povazay B, Hermann B, Hofer B, et al. Wide-field optical coherence tomography of the choroid in vivo. *Invest Ophthalmol Vis Sci*. 2009;50:1856–1863.
25. Motaghiannezam R, Schwartz DM, Fraser SE. In vivo human choroidal vascular pattern visualization using high-speed swept-source optical coherence tomography at 1060 nm. *Invest Ophthalmol Vis Sci*. 2012;53:2337–2348.
26. Sohrab M, Wu K, Fawzi AA. A pilot study of morphometric analysis of choroidal vasculature in vivo, using en face optical coherence tomography. *PLoS One*. 2012;7:26.
27. Alasil T, Ferrara D, Adhi M, et al. En face imaging of the choroid in polypoidal choroidal vasculopathy using swept-source optical coherence tomography. *Am J Ophthalmol*. 2015;159:634–643.
28. Ferrara D, Mohler KJ, Waheed N, et al. En face enhanced-depth swept-source optical coherence tomography features of chronic central serous chorioretinopathy. *Ophthalmology*. 2014;121:719–726.
29. Flores-Moreno I, Arias-Barquet L, Rubio-Caso MJ, Ruiz-Moreno JM, Duker JS, Caminal JM. En face swept-source optical coherence tomography in neovascular age-related macular degeneration. *Br J Ophthalmol*. 2015;99:1260–1267.
30. Potsaid B, Baumann B, Huang D, et al. Ultrahigh speed 1050nm swept source/Fourier domain OCT retinal and anterior segment imaging at 100,000 to 400,000 axial scans per second. *Opt Express*. 2010;18:20029–20048.
31. Choi W, Potsaid B, Jayaraman V, et al. Phase-sensitive swept-source optical coherence tomography imaging of the human retina with a vertical cavity surface-emitting laser light source. *Opt Lett*. 2013;38:338–340.
32. Klein T, Wieser W, Eigenwillig CM, Biedermann BR, Huber R. Megahertz OCT for ultrawide-field retinal imaging with a 1050 nm Fourier domain mode-locked laser. *Opt Express*. 2011;19:3044–3062.
33. Klein T, Wieser W, Reznicek L, Neubauer A, Kampik A, Huber R. Multi-MHz retinal OCT. *Biomed Opt Express*. 2013;4:1890–1908.
34. Kolb JP, Klein T, Kufner CL, Wieser W, Neubauer AS, Huber R. Ultra-widefield retinal MHz-OCT imaging with up to 100 degrees viewing angle. *Biomed Opt Express*. 2015;6:1534–1552.
35. Huber R, Wojtkowski M, Fujimoto JG. Fourier Domain Mode Locking (FDML): a new laser operating regime and applications for optical coherence tomography. *Opt Express*. 2006;14:3225–3237.
36. Srinivasan VJ, Adler DC, Chen Y, et al. Ultrahigh-speed optical coherence tomography for three-dimensional and en face imaging of the retina and optic nerve head. *Invest Ophthalmol Vis Sci*. 2008;49:5103–5110.
37. Reznicek L, Klein T, Wieser W, et al. Megahertz ultra-wide-field swept-source retina optical coherence tomography compared to current existing imaging devices. *Graefes Arch Clin Exp Ophthalmol*. 2014;252:1009–1016.
38. ANSI. *Safe Use of Lasers & Safe Use of Optical Fiber Communications*. Orlando, FL: American National Standard Institute Z136 Committee; 2000:168.
39. Hayreh SS. In vivo choroidal circulation and its watershed zones. *Eye*. 1990;4:273–289.
40. Mori K, Gehlbach PL, Yoneya S, Shimizu K. Asymmetry of choroidal venous vascular patterns in the human eye. *Ophthalmology*. 2004;111:507–512.
41. Neubauer A, Kernt M, Haritoglou C, Priglinger S, Kampik A, Ulbig M. Nonmydriatic screening for diabetic retinopathy by ultra-widefield scanning laser ophthalmoscopy (Optomap). *Graefes Arch Clin Exp Ophthalmol*. 2008;246:229–235.
42. Cheng SCK, Yap MKH, Goldschmidt E, Swann PG, Ng LHY, Lam CSY. Use of the Optomap with lid retraction and its sensitivity and specificity. *Clin Exp Optom*. 2008;91:373–378.
43. Zawadzki RJ, Fuller AR, Choi SS, Wiley DF, Hamann B, Werner JS. Correction of motion artifacts and scanning beam distortions in 3D ophthalmic optical coherence tomography imaging. *Proc. SPIE*. 2007;6426:642607.
44. Gross H, Blechinger F, Achtner B. Human eye. In: Gross H, ed. *Handbook of Optical Systems: Vol. 4: Survey of Optical Instruments*. Weinheim: WILEY-VCH Verlag GmbH & Co.; 2008:1–88.
45. Kajic V, Esmaeelpour M, Povazay B, Marshall D, Rosin PL, Drexler W. Automated choroidal segmentation of 1060 nm OCT in healthy and pathologic eyes using a statistical model. *Biomed Opt Express*. 2012;3:86–103.
46. Zhang L, Lee K, Niemeijer M, Mullins RF, Sonka M, Abramoff MD. Automated segmentation of the choroid from clinical SD-OCT. *Invest Ophthalmol Vis Sci*. 2012;53:7510–7519.
47. Duan L, Hong YJ, Yasuno Y. Automated segmentation and characterization of choroidal vessels in high-penetration optical coherence tomography. *Opt Express*. 2013;21:15787–15808.
48. Chen Q, Fan W, Niu S, Shi J, Shen H, Yuan S. Automated choroid segmentation based on gradual intensity distance in HD-OCT images. *Opt Express*. 2015;23:8974–8994.

Investigative Ophthalmology & Visual Science